

An Imaging Search for Circumstellar Companions of Sirius B

MILES LUCAS ¹, MICHAEL BOTTOM ², GARRETH RUANE ³, AND SAM RAGLAND ⁴

¹*Institute for Astronomy, University of Hawaii at Manoa, 2680 Woodlawn Dr, Honolulu, HI 96822, USA*

²*Institute for Astronomy, University of Hawaii at Hilo, 640 N Aohoku Pl, Hilo, HI 96720, USA*

³*Jet Propulsion Laboratory, California Institute of Technology, 4800 Oak Grove Dr, Pasadena, CA 91109, USA*

⁴*W.M. Keck Observatory, 65-1120 Mamalahoa Hwy, Waimea, HI 96743, USA*

ABSTRACT

We present deep imaging of Sirius B, the closest and brightest white dwarf. We use Keck/NIRC2 in Lp-band (3.776 μm) across 3 epochs in 2020 using the technique of angular differential imaging. We reach sub-Jupiter sensitivities and sub-AU separations, reaching 3.5 M_J at 0.25 AU down to a sensitivity of 0.6 M_J at 1.5 AU. The uncertainty in mass sensitivity is below 0.1 M_J due to the high-precision of the Sirius B system age. We do not detect any companions around Sirius B, consistent with previous studies.

1. INTRODUCTION

High-contrast imaging (HCI) is a powerful technique for discovering and characterizing exoplanets. Being able to probe the architecture, formation, and atmospheres of planets directly is necessary for advancing substellar companion formation and evolution theory. The process required to image a planet is daunting, however. The typical astrophysical flux ratios (contrast) for a Sun-Jupiter analog in the near-infrared (NIR) are $\sim 10^{-8}$, and for a Sun-Earth system are $\sim 10^{-10}$ (Traub & Oppenheimer 2010). Blackbody emission from exoplanets peaks in the infrared and is well into the Rayleigh-Jeans limit of the star, decreasing contrast compared to the visible or ultraviolet. In addition, the close angular separations of planets makes it difficult to detect them over the diffraction pattern of their host and other noise sources.

Typical targets for imaging are nearby young stars; the close proximity means the same angular separation probes a smaller physical separation, allowing for studies closer to solar-system scales. Younger exoplanets are hotter and therefore brighter, reducing the flux ratio between the planet and its host star. Another way to reduce contrast would be to make the star fainter, which is precisely what happens in the latest stages of stellar evolution during the white dwarf cooling sequence. When intermediate mass stars (1 M_\odot to 8 M_\odot) eventu-

ally exit the main-sequence (MS) they expand up to ~ 100 s of stellar radii during the red giant branch (RGB) phase. This expansion will engulf planets within the star's Roche limit. Then, during the asymptotic giant branch (AGB) phase, mass loss will adiabatically expand any orbits. Finally, once the star becomes a white dwarf it begins cooling, which reduces its luminosity by 3 to 4 orders of magnitude compared to its MS progenitor. The faintness, broad spectral lines, and expanded orbits make white dwarfs exceptionally challenging for the transit photometry and radial velocity methods. However, the reduced contrast due to the faintness of the star, and the expanded separation of planets both benefit imaging.

2. POST-MS EVOLUTION

There is limited knowledge of planetary systems around evolved stars. Burleigh et al. (2002); Veras (2016) suggest exoplanets on initially wide (>5 AU) orbits around intermediate mass stars will survive expansion during the RGB phase. Close-in planets that escape the Roche limit of the expanding red giant can still be shredded by tidal forces, although the tidal forces on planets that readily escape engulfment are negligible (Nordhaus & Spiegel 2013). During the AGB phase, stellar mass loss will adiabatically expand the orbit of the planet by a maximum factor of $M_{*,\text{MS}}/M_{*,\text{WD}}$ (Jeans 1924). In addition to *first-generation* planets there are potential methods for *second-generation* planets to form after the violent RGB and AGB phases (Perets 2010).

The first search for substellar companions around white dwarfs was conducted by Probst (1983) by searching for infrared (IR) excess in their spectral energy distributions (SED) using broadband photometry. They found no companions around the ~ 100 white dwarfs they studied. The same method was applied by Zuckerman & Becklin (1987) who found excess IR emission around white dwarf G29-38. Eventually this excess was determined to be from a dust disk (Telesco et al. 1990) and the current interpretation associates the dust with accretion onto the white dwarf, polluting the stellar atmosphere (Koester et al. 1997).

To date, there has been no direct images of an exoplanet around a white dwarf, although a brown dwarf with a mass of $7 M_J$ on a wide 2500 AU orbit was imaged around a single white dwarf (WD 0806-661B) using Spitzer (Luhman et al. 2011). The “Degenerate Objects around Degenerate Objects” survey (DODO; Hogan et al. 2009) observed 29 white dwarfs with Gemini/NIRI and VLT/ISAAC, reaching an average upper limit around $\sim 8 M_J$ beyond 35 AU. The young white dwarf GD 50 was observed using the extreme AO instrument SPHERE at the VLT (Xu et al. 2015), reaching sensitivity limits of $4 M_J$ at 6.2 AU.

3. SIRIUS B AND THE SIRIUS SYSTEM

A particularly fascinating such target is Sirius B, the closest and brightest white dwarf. The Sirius system is the 7th closest to the sun at 2.6 pc, consisting of Sirius A, a -1.35 magnitude A1Vm star known for being the brightest, and Sirius B, a DA2 white dwarf with a 50 yr orbit (Bond et al. 2017; Gaia Collaboration et al. 2018). As mentioned previously, the proximity and faintness of Sirius B (compared to a MS star) make it compelling for imaging, and additionally it is a young system (~ 225 Myr), further reducing the predicted contrast necessary to image a planetary companion.

The age of the Sirius system is has much better precision than most stars ($\sim 1\%$ vs. $\sim 10\%$ or worse), which is paramount for estimating the mass of a companion from photometry. Because Sirius B is relatively young, the age uncertainty exponentially affects planet mass uncertainty due to the rapid cooling of young planets (< 1 Gyr) (Fortney et al. 2010). The high system age precision is primarily derived from the well-defined dynamical masses of the binary. With well-known masses, isochrones and stellar evolution codes can be combined to pinpoint the age. The dynamical masses are determined through astrometric studies; the first study of Sirius was performed by Bessel (1844), who recognized wobbles in the proper motion of Sirius A caused by a “dark satellite”. This dark satellite was visually con-

firmed in Bond (1862) as Sirius B. Adams (1915) took the first spectral measurements of Sirius B and found it to be similar to a MS early A-type star, despite its faintness, which we now know to be typical of white dwarf spectra.

Initial astrometric perturbations suggested a 50 year orbital period (Auwers 1864) for Sirius B. van den Bos (1960); Gatewood & Gatewood (1978) were the first to estimate dynamic masses using compilations of photographic plates from Lick and Yerkes observatories. Bond et al. (2017) greatly refined the orbital solution using a compilation of historical data and Hubble Space Telescope (HST) data, which gave dynamical masses of $(2.063 \pm 0.023) M_\odot$ and $(1.018 \pm 0.011) M_\odot$ for A and B, respectively.

To find the total age of Sirius B, Bond et al. (2017) used isochrones to constrain the cooling age (126 Myr), first. Applying the initial-final mass relation (IFMR) of white dwarfs (Cummings et al. 2016) the estimated progenitor mass of Sirius B is between $5 M_\odot$ to $5.6 M_\odot$, which, when combined with stellar evolution codes, yielded total system ages between 226 Myr to 228 Myr with an uncertainty of about ± 10 Myr (Bond et al. 2017).

A companion around Sirius B would be affected by the orbit of Sirius A, and this constrained three-body system has been studied numerically (Holman & Wiegert 1999). Bond et al. (2017) calculate the longest period stable companion around Sirius B is 1.79 yr, which corresponds to a 1.5 AU circular orbit.

The first modern imaging study searching for companions around Sirius B was Schroeder et al. (2000) who used the HST wide-field planetary camera (WFPC) at $1 \mu\text{m}$. Around the same time Kuchner & Brown (2000) searched in a narrower field of view (FOV) with HST/NICMOS at $1 \mu\text{m}$. These studies combined had a sensitivity down to $\sim 10 M_J$ at 5.3 AU ($2''$). Bonnet-Bidaud & Pantin (2008) used the ground-based ESO/ADONIS instrument in J, H, and Ks-band and reached a sensitivity of $\sim 30 M_J$ at 7.9 AU ($3''$). Skemer & Close (2011) used mid-IR (up to $10 \mu\text{m}$) observations from Gemini/T-ReCs which ruled out evidence for any infrared excess around Sirius B. Thalmann et al. (2011) used Subaru/IRCS at $4.05 \mu\text{m}$ reaching detection sensitivities of $6 M_J$ to $12 M_J$ at $1''$. Recently, Pathak et al. (2021) took simultaneous mid-IR observations ($10 \mu\text{m}$) at VLT/VISIR of Sirius A (through a coronagraph) and B. Because of the simultaneous observation, their contrast depended on which region of the FOV was tested. Their average sensitivity is $\sim 2.5 M_J$ at 1 AU, and their best sensitivity (from the “inner” region) is $\sim 1.5 M_J$ at 1 AU.

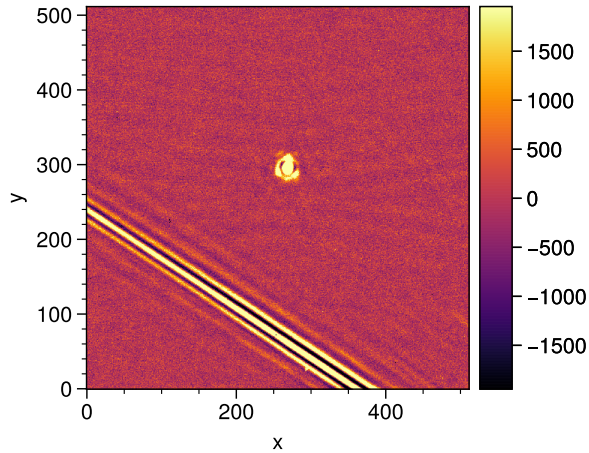


Figure 1. A diffraction spike sweeping across a calibrated science frame of Sirius B from the first epoch. This shows the strong scattered light effects of Sirius A and how they affect the FOV of Sirius B $11''$ away.

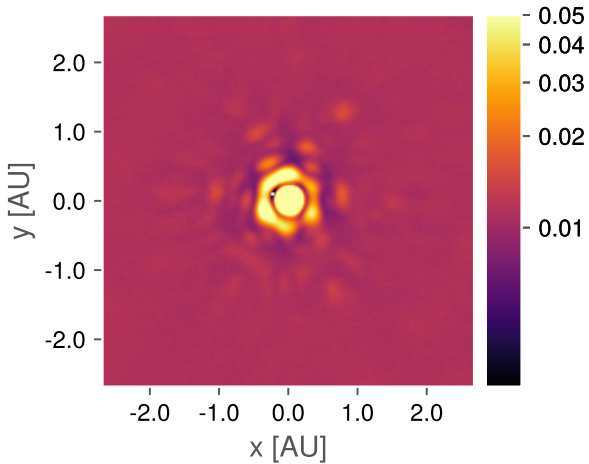


Figure 2. The median frame from the second epoch showing the instrumental PSF. The inner core has a FWHM of ~ 76 mas. The speckle pattern is shown in the blobs surrounding the first ring, with roughly 6-way radial symmetry corresponding to the hexagonal shape of the primary mirror.

In this work we report direct images of Sirius B with Keck/NIRC2. [section 4](#) describes our target and observing strategy, [section 5](#) describes the processing and analysis techniques used, [section 6](#) describes our results and we conclude with [section 7](#).

4. OBSERVATIONS

Despite Sirius B being the brightest white dwarf in the sky, it is still 10 magnitudes fainter than Sirius A, making it a technically challenging target, especially on

ground-based telescopes. We directly imaged Sirius B with Keck/NIRC2 in Lp-band ($3.776\mu\text{m}$) across three epochs in 2020 ([Table 1](#)). Our first attempt to observe Sirius B failed due to the strong scattered light from Sirius A. The adaptive optics (AO) calibration failed when the scattered light from Sirius A would sweep into the FOV of the wavefront sensor (WFS). Similarly, trying to deploy the focal-plane vortex coronagraph ([Serabyn et al. 2017](#)) failed when the coronagraphic pointing control algorithm, QACITS ([Huby et al. 2017](#)), performed erratically in the presence of the scattered light. [Vigan et al. \(2015, §2\)](#) reported similar issues in their attempts to image Sirius B coronagraphically. In order to overcome these obstacles, we decided to try using Sirius A as the AO guide star and off-axis guiding to Sirius B.

The Keck AO system ([Wizinowich et al. 2000](#)) was saturated by Sirius A, so we attenuated the flux using a narrow laser-line filter to avoid saturating the WFS. While still bright (appearing like a ~ 5 magnitude star on the WFS), this was enough attenuation to close the AO loop. From here, we slewed off-axis using the separations and position angles calculated in [Table 1](#) from the orbital parameters in [Bond et al. \(2017\)](#). In this mode, we noticed higher than usual drift in the focal plane, requiring manually recentering the target every 5 or 10 minutes. We tried deploying the vortex coronagraph along with QACITS, but the diffracted light from Sirius A made QACITS unstable, so we decided to forego any coronagraphy for the remaining observations.

During each observation, we took dark frames and sky flat frames for calibration. We also disabled the field rotator, which caused the FOV to rotate throughout the night for angular differential imaging (ADI; [Marois et al. 2006](#)).

5. ANALYSIS

5.1. Pre-processing

The raw images from NIRC2 required pre-processing before analyzing them for companions. For each epoch we applied a flat correction using calibration frames captured during observing. We also removed bad pixels using a combination of L.A.Cosmic ([van Dokkum 2001](#)) and an adaptive sigma-clipping algorithm. We removed sky background using a high-pass median filter with a box size of 31 pixels. For both the November epochs we tried exploiting the large focal plane drifts by dithering between two positions in order to simplify background subtraction, but this ended up performing worse than the high-pass filter. At this point frames were manually selected to remove bad frames, especially those with diffraction spikes from Sirius A within a few hundred pixels, like in [Figure 1](#). Then, each good frame was

Table 1. Observing parameters for the three epochs of data. All observations were carried out using the NIRC2 Lp-band filter. Observation time is based on the frames that were selected for processing. Seeing values are measured at 0.5 μm using a differential image motion monitor (DIMM) and averaged over the observing session. Seeing values, temperature, and water vapor measurements are all provided by the Maunakea weather center forecast archive.

Date observed	Sirius B offset (")	Sirius B PA (°)	Obs. time (hr)	FOV rotation (°)	FWHM (mas)	Seeing (")	Temp (°C)	PWV (mm)
2020-02-04	11.20	67.90	1.44	60.1	79.9	0.936	0.0	0.7
2020-11-21	11.27	66.42	2.91	91.4	76.4	0.871	0.75	3.5
2020-11-28	11.27	66.38	2.44	80.4	82.2	1.23	-1.5	3.0

co-registered to sub-pixel accuracy using the algorithm presented in Guizar-Sicairos et al. (2008), followed by fitting each frame with a Gaussian PSF to reach floating-point centroid accuracy.

The co-registered frames are then shifted to the center of the FOV. Lastly the frames were cropped to the inner 200 pixels and stacked into data cubes for each epoch. With a pixel scale of 10 mas the crop corresponds to a maximum separation of 1" or a projected separation of 2.7 AU. We also measure the parallactic angle of each frame, including corrections for distortion effects following Yelda et al. (2010). For each epoch, we measure the full-width at half-maximum (FWHM) of the stellar PSF for use in post-processing by fitting a bivariate Gaussian model to the median frame from each data cube (Figure 2). All of the pre-processing code is available in Jupyter notebooks in a GitHub repository (<https://github.com/mileslucas/sirius-b>) and the pre-processed data cubes and parallactic angles are available on Zenodo: [10.5281/zenodo.5115225](https://zenodo.org/record/5115225).

5.2. Post-processing

By taking data with the field rotator disabled (ADI), the point-spread function (PSF) will not appear to rotate while any potential companion will appear to rotate. This reduces the probability of subtracting companion signal when we subtract the stellar PSF model. After subtraction, the frames are derotated by their parallactic angle and combined with a weighted sum (Bottom et al. 2017), which reduces the pixel-to-pixel noise as the number of frames in the data cube increases.

For this analysis we used four ADI algorithms for modeling and subtracting the stellar PSF: median subtraction (Marois et al. 2006), principal component analysis (PCA, also referred to as KLIP; Soummer et al. 2012), non-negative matrix factorization (NMF; Ren et al. 2018), and fixed-point greedy disk subtraction (GreeDS; Pairet et al. 2019b, 2020). The median subtraction and PCA methods were also applied in an annular method, where we modeled the PSF in annuli of

increasing separation, discarding frames which have not rotated at least 0.5 FWHM (Marois et al. 2006).

We used three metrics for determining the performance of each algorithm, the signal-to-noise ratio (S/N) significance map, the standardized trajectory intensity mean map (STIM map; Pairet et al. 2019a), and the contrast curve. The significance and STIM maps assign a likelihood to each pixel for the presence of a companion using different assumptions of the residual statistics. The contrast curve determines the sensitivity of a 5σ statistical detection through repeated injection and retrieval of planetary signal as processed by one of the ADI algorithms above. We calculate both the Gaussian contrast and the Student-t corrected contrast, which accounts for the small-sample statistics in each annulus (Mawet et al. 2014). The collapsed residual frames along with the above metrics for each algorithm for each epoch are in Appendix A.

A common problem when using subspace-driven post-processing algorithms like PCA, NMF, or GreeDS is choosing the size of the subspace (i.e., the number of components). For PCA, NMF, and GreeDS algorithms, we created residual cubes for increasing number of components, from 1 to 10. We chose 10 as the max number of components because we saw a dramatic decline in contrast sensitivity after the first few components (Figure 12). In our analysis we employed the STIM largest intensity mask map (SLIM map; Pairet 2020) as an ensemble statistic. The SLIM map calculates the average STIM map from many residual cubes along with the average mask of the N most intense pixels in each STIM map. A real companion ought to be present in many different residual cubes from the same dataset, so this ensemble approach can give us a probability map without predetermining the number of components. The collapsed residual frames, average STIM map, SLIM map, and contrast curves for each epoch for each of the above algorithms are in Appendix A.

All of the ADI algorithms and metrics are implemented in the open-source Julia package ADI.jl (Lucas

& Bottom 2020). All of the code for the ADI processing in this paper, including the scripts for each figure produced are in a GitHub repository in Jupyter notebooks and Julia scripts (<https://github.com/mileslucas/sirius-b>).

6. RESULTS

We determined the best-performing algorithms for each epoch using the contrast curves described in [section 5](#). For the first two epochs full-frame median subtraction had the best contrast at almost all separations. For the last epoch annular PCA subtraction with 2 principal components and a rotation threshold of 0.5 FWHM produced the best contrast at close separations (0.2'' to 0.4'') and had similar performance to other algorithms beyond 0.4''. The innermost annulus from this algorithm has invalid contrast (>1) and is not shown. The collapsed residual frames from each epoch are shown in [Figure 3](#), along with the Gaussian significance maps ([Figure 4](#)) and STIM maps ([Figure 5](#)).

The reduced images do not show consistent or significant evidence for a substellar companion. The STIM probability maps for the 2020-11-21 and 2020-11-28 epochs suggest evidence for some blobs $\sim 0.13''$ (~ 1.6 FWHM) from the center. The lack of evidence in the February epoch and the significance maps as well as the proximity to the central star both reduce the probability of these blobs being true companions. Nonetheless, we estimated astrometry for blobs from each epoch ([Table 2](#)) and tried fitting Keplerian orbits using the “Orbits for the Impatient” algorithm (OFTI; [Blunt et al. 2017](#)). We generated 10^4 orbits, none of which managed to contain the points from each epoch ([Appendix B](#)). We take this as direct evidence against the blobs being substellar companions of any kind.

It is interesting to note the morphology of the innermost $\sim 0.4''$ in the frames produced by GreeDS and NMF. Both of these algorithms usually outperform traditional median and PCA subtraction for disk imaging. In the frames from each epoch, but particularly in the two November epochs, a symmetric “barbell” shape can be seen which is similar to other disk images (e.g., [fig. 7 Norris et al. 2014](#)). Due to the nature of high-contrast imaging, it is difficult to differentiate systematic noise from real signal in the speckle-limited regime, in addition there is no prior evidence for a circumstellar disk from IR excess. Follow-up work in the visible (e.g., Subaru/VAMPIRES, VLT/SPHERE) may be able to image such a disk.

The contrast maps from the best performing algorithm for each reduction are shown in [Figure 6](#). We determine the limiting sensitivities in terms of the plan-

etary mass by first calculating the contrast-limited magnitude using an Lp-band magnitude for Sirius B of 9.1 (adapted from [Bonnet-Bidaud & Pantin 2008](#)). Then we use an age of 225 Myr to interpolate the planetary mass using the AMES-Cond evolutionary grid and atmosphere models ([Allard et al. 2012](#)). The high precision of the Sirius system’s age (see [section 1](#)) reduces uncertainty when interpolating planetary mass from the evolutionary grids. The best performing epoch was on the night of 2020-11-21, which managed to reach an exceptional sensitivity of 3.5 M_J at 0.25 AU (0.09'') in the speckle limited regime and ultimately 0.6 M_J at 1.5 AU (0.38'') in the background limited regime.

7. CONCLUSIONS

In closing, the Sirius system is one of the most well studied in history, with Sirius B being the target of companion searches from the visible to the IR. While it is highly unlikely a first-generation planet survived post-MS evolution, imaging efforts have gradually increased the sensitivity to second-generation planets. In this work we present high-contrast images of Sirius B in the near-IR. Our sensitivity limits are the best that have been reached for Sirius B, reaching 0.6 M_J at 1.5 AU, the outer limit for dynamically stable orbits. Our observations also show how the high precision of the parameters of the Sirius system directly benefit the sensitivity to planets. Particularly, the low age uncertainty of Sirius B keeps our mass uncertainty below 0.1 M_J . Despite the high sensitivity of this study, we found no appreciable evidence for a companion around Sirius B, consistent with previous results. This non-detection furthers evidence against a second-generation planet migrating or forming within the Sirius system ([Vigan et al. 2015](#)).

We have published alongside this work the entire codebase used for pre-processing and reducing the data, and for generating every figure in this manuscript. We have also published our reduced datasets under an open license. We hope that this improves the reproducibility of the work as well as providing data for testing new ADI algorithms.

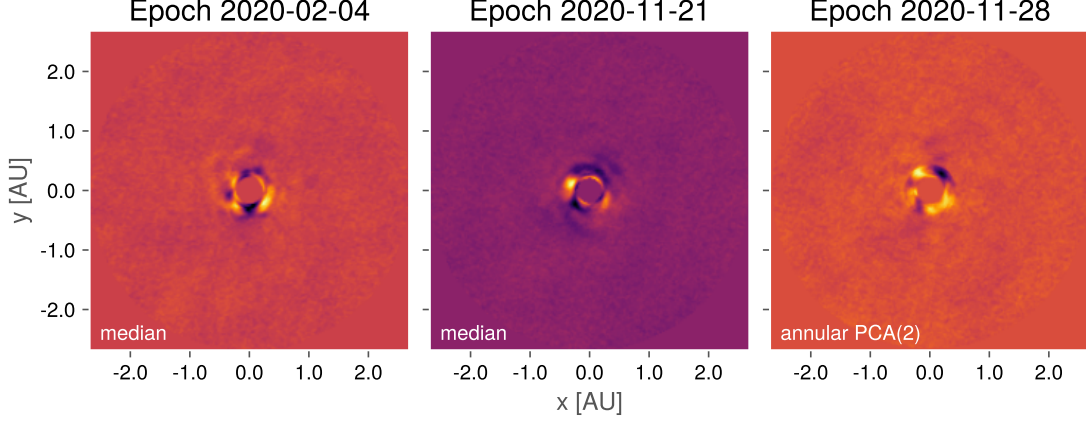


Figure 3. The flat residuals of each epoch after PSF subtraction, derotating, and collapsing. The inner full-width at half-maximum (FWHM) is masked out for each frame.

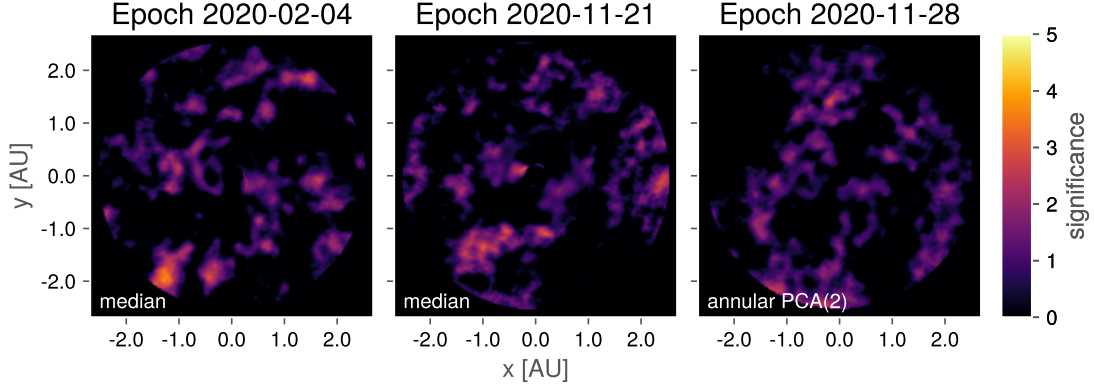


Figure 4. The *significance* maps for each epoch accounting for small sample statistics (Mawet et al. 2014). Typically a critical value for detection is 5. The inner full-width at half-maximum (FWHM) is masked out for each map.

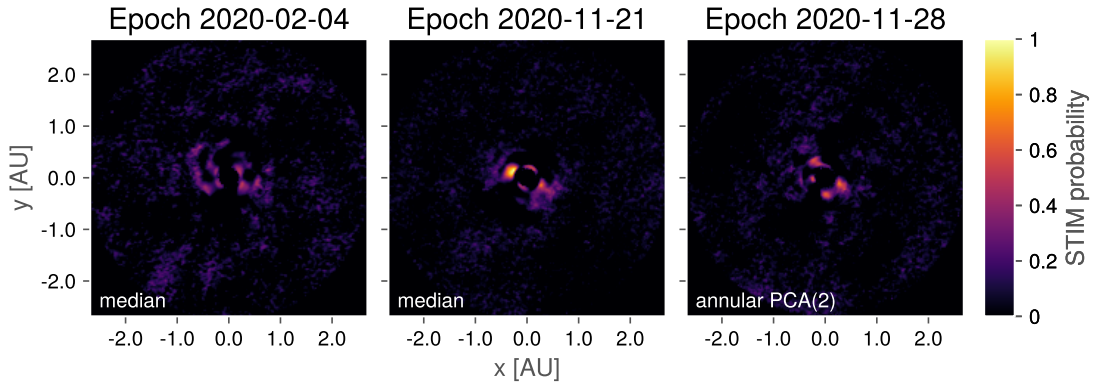


Figure 5. The STIM maps for each epoch calculated from the residual cube. The STIM probability has a typical cutoff threshold of 0.5 for significant detections. The inner full-width at half-maximum (FWHM) is masked out for each map.

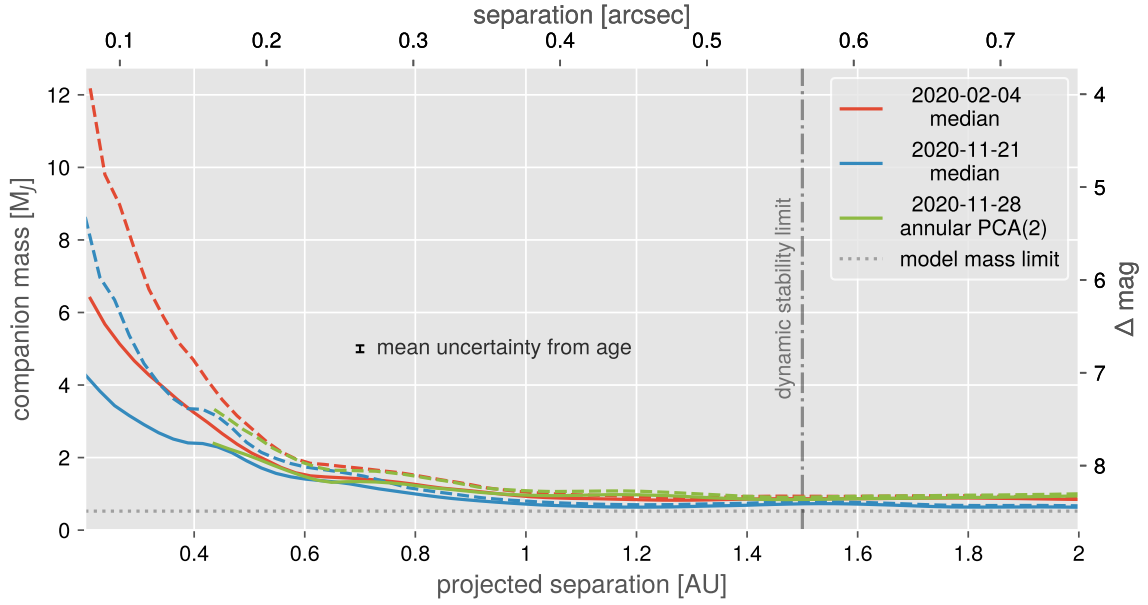


Figure 6. The contrast curves for the best performing algorithm from each epoch. The solid lines are the Gaussian 5σ contrast curves and the dashed lines are the Student-t corrected curves. The mean uncertainty from the total system age (~ 10 Myr) is shown by a lone error bar. In addition, the expected upper limit for orbital separation of a stable orbit of 1.5 AU is plotted as a vertical dashed line. The companion mass values are interpolated from the AMES-Cond grid. The lower mass limit (upper magnitude limit) of these models is plotted in a light-gray horizontal dashed line. The annular PCA curve is cut off because the contrast in the innermost annulus was greater than 1.

ACKNOWLEDGMENTS

The data presented herein were obtained at the W. M. Keck Observatory, which is operated as a scientific partnership among the California Institute of Technology, the University of California and the National Aeronautics and Space Administration. The Observatory was made possible by the generous financial support of the W. M. Keck Foundation. The authors wish to recognize and acknowledge the very significant cultural role and reverence that the summit of Maunakea has always had within the indigenous Hawaiian community. We are most fortunate to have the opportunity to conduct observations from this mountain.

Facility: Keck:II (NIRC2)

Software: ADI.jl (Lucas & Bottom 2020), astropy (Collaboration et al. 2013; Astropy Collaboration et al. 2018), Julia (Bezanson et al. 2017), numpy (Harris et al. 2020), scikit-image (Walt et al. 2014),

REFERENCES

- Adams, W. S. 1915, Publications of the Astronomical Society of the Pacific, 27, 236, doi: [10.1086/122440](https://doi.org/10.1086/122440)
- Allard, F., Homeier, D., & Freytag, B. 2012, Philos Trans A Math Phys Eng Sci, 370, 2765, doi: [10.1098/rsta.2011.0269](https://doi.org/10.1098/rsta.2011.0269)
- Astropy Collaboration, Price-Whelan, A. M., Sipőcz, B. M., et al. 2018, The Astronomical Journal, 156, 123, doi: [10.3847/1538-3881/aabc4f](https://doi.org/10.3847/1538-3881/aabc4f)
- Auwers, A. 1864, Monthly Notices of the Royal Astronomical Society, 25, 38. <https://ui.adsabs.harvard.edu/abs/1864MNRAS..25...38A>
- Bessel, F. W. 1844, Monthly Notices of the Royal Astronomical Society, 6, 136, doi: [10.1093/mnras/6.11.136](https://doi.org/10.1093/mnras/6.11.136)
- Bezanson, J., Edelman, A., Karpinski, S., & Shah, V. B. 2017, SIAM Rev., 59, 65, doi: [10.1137/141000671](https://doi.org/10.1137/141000671)
- Blunt, S., Nielsen, E. L., De Rosa, R. J., et al. 2017, The Astronomical Journal, 153, 229, doi: [10.3847/1538-3881/aa6930](https://doi.org/10.3847/1538-3881/aa6930)
- Bond, G. 1862, Astronomische Nachrichten, 57, 131. <https://ui.adsabs.harvard.edu/abs/1862AN.....57..131B>
- Bond, H. E., Schaefer, G. H., Gilliland, R. L., et al. 2017, The Astrophysical Journal, 840, 70, doi: [10.3847/1538-4357/aa6af8](https://doi.org/10.3847/1538-4357/aa6af8)
- Bonnet-Bidaud, J.-M., & Pantin, E. 2008, A&A, 489, 651, doi: [10.1051/0004-6361:20078937](https://doi.org/10.1051/0004-6361:20078937)
- Bottom, M., Ruane, G., & Mawet, D. 2017, Research Notes of the American Astronomical Society, 1, 30, doi: [10.3847/2515-5172/aa9d18](https://doi.org/10.3847/2515-5172/aa9d18)
- Burleigh, M. R., Clarke, F. J., & Hodgkin, S. T. 2002, Monthly Notices of the Royal Astronomical Society, 331, L41, doi: [10.1046/j.1365-8711.2002.05417.x](https://doi.org/10.1046/j.1365-8711.2002.05417.x)
- Collaboration, A., Robitaille, T. P., Tollerud, E. J., et al. 2013, Astronomy and Astrophysics, 558, A33, doi: [10.1051/0004-6361/201322068](https://doi.org/10.1051/0004-6361/201322068)
- Cummings, J. D., Kalirai, J. S., Tremblay, P. E., & Ramirez-Ruiz, E. 2016, The Astrophysical Journal, 818, 84, doi: [10.3847/0004-637X/818/1/84](https://doi.org/10.3847/0004-637X/818/1/84)
- Fortney, J. J., Baraffe, I., & Militzer, B. 2010, Giant Planet Interior Structure and Thermal Evolution. <https://ui.adsabs.harvard.edu/abs/2010exop.book..397F>
- Gaia Collaboration, Brown, A. G. A., Vallenari, A., et al. 2018, Astronomy & Astrophysics, Volume 616, id.A1, <NUMPAGES>22</NUMPAGES> pp., 616, A1, doi: [10.1051/0004-6361/201833051](https://doi.org/10.1051/0004-6361/201833051)
- Gatewood, G. D., & Gatewood, C. V. 1978, The Astrophysical Journal, 225, 191, doi: [10.1086/156480](https://doi.org/10.1086/156480)
- Guizar-Sicairos, M., Thurman, S. T., & Fienup, J. R. 2008, Opt. Lett., OL, 33, 156, doi: [10.1364/OL.33.000156](https://doi.org/10.1364/OL.33.000156)
- Harris, C. R., Millman, K. J., van der Walt, S. J., et al. 2020, Nature, 585, 357, doi: [10.1038/s41586-020-2649-2](https://doi.org/10.1038/s41586-020-2649-2)
- Hogan, E., Burleigh, M. R., & Clarke, F. J. 2009, Monthly Notices of the Royal Astronomical Society, 396, 2074, doi: [10.1111/j.1365-2966.2009.14565.x](https://doi.org/10.1111/j.1365-2966.2009.14565.x)
- Holman, M. J., & Wiegert, P. A. 1999, The Astronomical Journal, 117, 621, doi: [10.1086/300695](https://doi.org/10.1086/300695)
- Huby, E., Baudoz, P., Mawet, D., & Absil, O. 2017, The Astronomical Journal, 153, 43, doi: [10.3847/1538-3881/153/1/43](https://doi.org/10.3847/1538-3881/153/1/43)
- Jeans, J. H. 1924, Monthly Notices of the Royal Astronomical Society, 85, 2, doi: [10.1093/mnras/85.1.2](https://doi.org/10.1093/mnras/85.1.2)
- Koester, D., Provencal, J., & Shipman, H. L. 1997, Astronomy and Astrophysics, v.320, p.L57-L59, 320, L57. <https://ui.adsabs.harvard.edu/abs/1997A%26A...320L..57K/abstract>

- Kuchner, M. J., & Brown, M. E. 2000, Publications of the Astronomical Society of the Pacific, 112, 827, doi: [10.1086/316581](https://doi.org/10.1086/316581)
- Lucas, M., & Bottom, M. 2020, Journal of Open Source Software, 5, 2843, doi: [10.21105/joss.02843](https://doi.org/10.21105/joss.02843)
- Luhman, K. L., Burgasser, A. J., & Bochanski, J. J. 2011, The Astrophysical Journal, 730, L9, doi: [10.1088/2041-8205/730/1/L9](https://doi.org/10.1088/2041-8205/730/1/L9)
- Marois, C., Lafrenière, D., Doyon, R., Macintosh, B., & Nadeau, D. 2006, The Astrophysical Journal, 641, 556, doi: [10.1086/500401](https://doi.org/10.1086/500401)
- Mawet, D., Milli, J., Wahhaj, Z., et al. 2014, ApJ, 792, 97, doi: [10.1088/0004-637X/792/2/97](https://doi.org/10.1088/0004-637X/792/2/97)
- Nordhaus, J., & Spiegel, D. S. 2013, Monthly Notices of the Royal Astronomical Society, 432, 500, doi: [10.1093/mnras/stt569](https://doi.org/10.1093/mnras/stt569)
- Norris, B., Tuthill, P., Jovanovic, N., et al. 2014, arXiv e-prints, arXiv:1405.7426. <https://ui.adsabs.harvard.edu/abs/2014arXiv1405.7426N>
- Pairet, B. 2020, PhD thesis, UCL - Université Catholique de Louvain. <https://dial.uclouvain.be/pr/boreal/object/boreal:240621>
- Pairet, B., Cantalloube, F., Gomez Gonzalez, C. A., Absil, O., & Jacques, L. 2019a, Monthly Notices of the Royal Astronomical Society, 487, 2262, doi: [10.1093/mnras/stz1350](https://doi.org/10.1093/mnras/stz1350)
- Pairet, B., Cantalloube, F., & Jacques, L. 2019b, arXiv:1812.01333 [astro-ph]. <http://arxiv.org/abs/1812.01333>
- . 2020, arXiv:2008.05170 [astro-ph]. <http://arxiv.org/abs/2008.05170>
- Pathak, P., de la Roche, D. J. M. P. d., Kasper, M., et al. 2021, arXiv:2104.13032 [astro-ph]. <http://arxiv.org/abs/2104.13032>
- Perets, H. B. 2010, arXiv e-prints, arXiv:1001.0581. <https://ui.adsabs.harvard.edu/abs/2010arXiv1001.0581P>
- Probst, R. G. 1983, The Astrophysical Journal Supplement Series, 53, 335, doi: [10.1086/190893](https://doi.org/10.1086/190893)
- Ren, B., Pueyo, L., Zhu, G. B., Debes, J., & Duchêne, G. 2018, The Astrophysical Journal, 852, 104, doi: [10.3847/1538-4357/aaa1f2](https://doi.org/10.3847/1538-4357/aaa1f2)
- Schroeder, D. J., Golimowski, D. A., Bruckardt, R. A., et al. 2000, The Astronomical Journal, 119, 906, doi: [10.1086/301227](https://doi.org/10.1086/301227)
- Serabyn, E., Huby, E., Matthews, K., et al. 2017, The Astronomical Journal, 153, 43, doi: [10.3847/1538-3881/153/1/43](https://doi.org/10.3847/1538-3881/153/1/43)
- Skemer, A. J., & Close, L. M. 2011, The Astrophysical Journal, 730, 53, doi: [10.1088/0004-637X/730/1/53](https://doi.org/10.1088/0004-637X/730/1/53)
- Soummer, R., Pueyo, L., & Larkin, J. 2012, The Astrophysical Journal Letters, 755, L28, doi: [10.1088/2041-8205/755/2/L28](https://doi.org/10.1088/2041-8205/755/2/L28)
- Telesco, C. M., Joy, M., & Sisk, C. 1990, The Astrophysical Journal, 358, L17, doi: [10.1086/185769](https://doi.org/10.1086/185769)
- Thalmann, C., Usuda, T., Kenworthy, M., et al. 2011, The Astrophysical Journal, 732, L34, doi: [10.1088/2041-8205/732/2/L34](https://doi.org/10.1088/2041-8205/732/2/L34)
- Traub, W. A., & Oppenheimer, B. R. 2010, Exoplanets, 111. <http://adsabs.harvard.edu/abs/2010exop.book..111T>
- van den Bos, W. H. 1960, Journal des Observateurs, 43, 145. <https://ui.adsabs.harvard.edu/abs/1960JO....43..145V>
- van Dokkum, P. G. 2001, Publications of the Astronomical Society of the Pacific, 113, 1420, doi: [10.1086/323894](https://doi.org/10.1086/323894)
- Veras, D. 2016, Royal Society Open Science, 3, 150571, doi: [10.1098/rsos.150571](https://doi.org/10.1098/rsos.150571)
- Vigan, A., Gry, C., Salter, G., et al. 2015, Monthly Notices of the Royal Astronomical Society, 454, 129, doi: [10.1093/mnras/stv1928](https://doi.org/10.1093/mnras/stv1928)
- Walt, S. v. d., Schönberger, J. L., Nunez-Iglesias, J., et al. 2014, PeerJ, 2, e453, doi: [10.7717/peerj.453](https://doi.org/10.7717/peerj.453)
- Wizinowich, P. L., Acton, D. S., Lai, O., et al. 2000, 4007, 2, doi: [10.1117/12.390368](https://doi.org/10.1117/12.390368)
- Xu, S., Ertel, S., Wahhaj, Z., et al. 2015, Astronomy & Astrophysics, Volume 579, id.L8, <NUMPAGES>5</NUMPAGES> pp., 579, L8, doi: [10.1051/0004-6361/201526179](https://doi.org/10.1051/0004-6361/201526179)
- Yelda, S., Lu, J. R., Ghez, A. M., et al. 2010, The Astrophysical Journal, Volume 725, Issue 1, pp. 331-352 (2010)., 725, 331, doi: [10.1088/0004-637X/725/1/331](https://doi.org/10.1088/0004-637X/725/1/331)
- Zuckerman, B., & Becklin, E. E. 1987, Nature, 330, 138, doi: [10.1038/330138a0](https://doi.org/10.1038/330138a0)

APPENDIX

A. ADI PROCESSING RESULTS

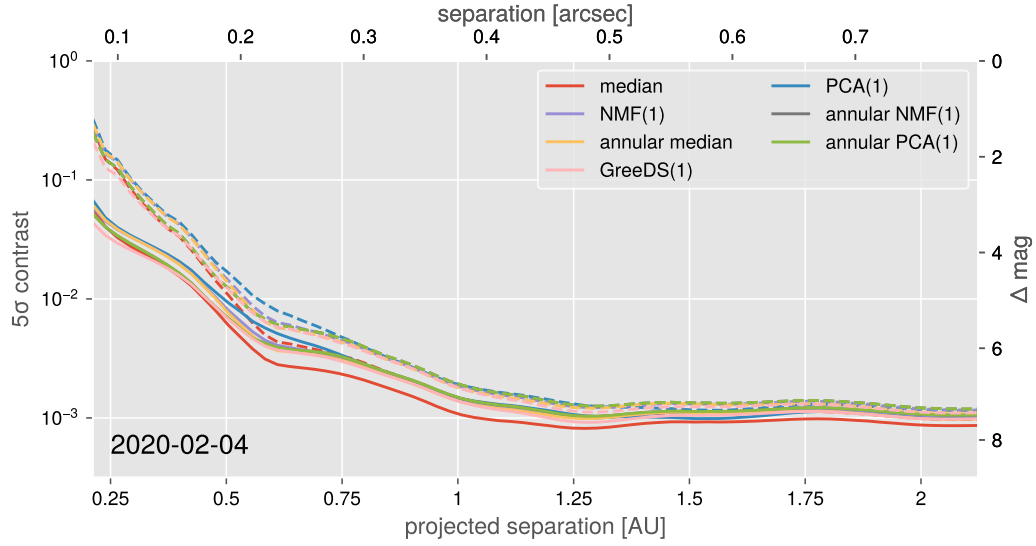


Figure 7. 5σ contrast curves from every ADI algorithm for the first epoch. Both the Gaussian (solid lines) and Student-t corrected (dashed lines) contrast curves are shown.

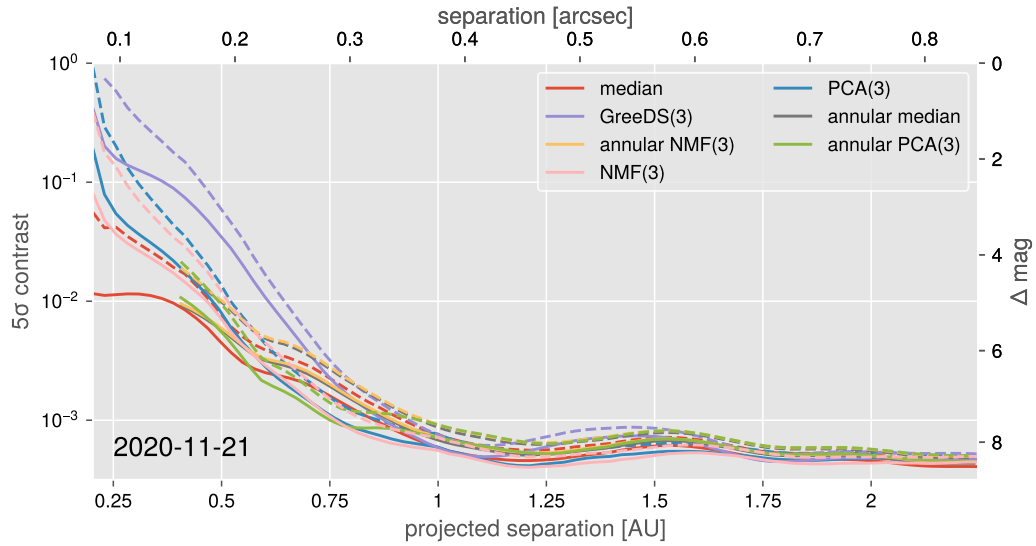


Figure 8. 5σ contrast curves from every ADI algorithm for the second epoch. Both the Gaussian (solid lines) and Student-t corrected (dashed lines) contrast curves are shown.

Fig. Set 10. ADI processing results

Fig. Set 11. PCA, NMF, and GreeDS mosaics

Fig. Set 12. PCA, NMF, and GreeDS results

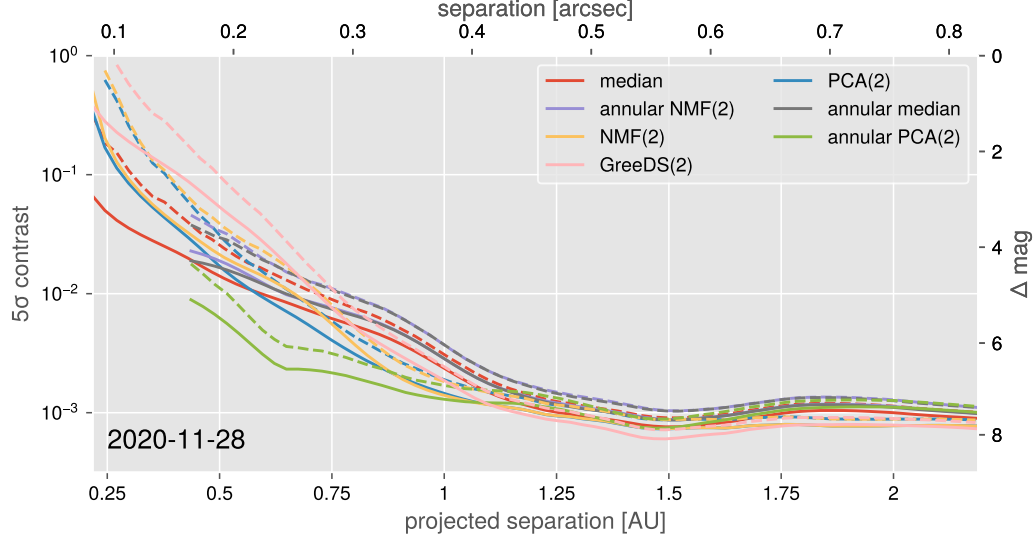


Figure 9. 5σ contrast curves from every ADI algorithm for the third epoch. Both the Gaussian (solid lines) and Student-t corrected (dashed lines) contrast curves are shown.

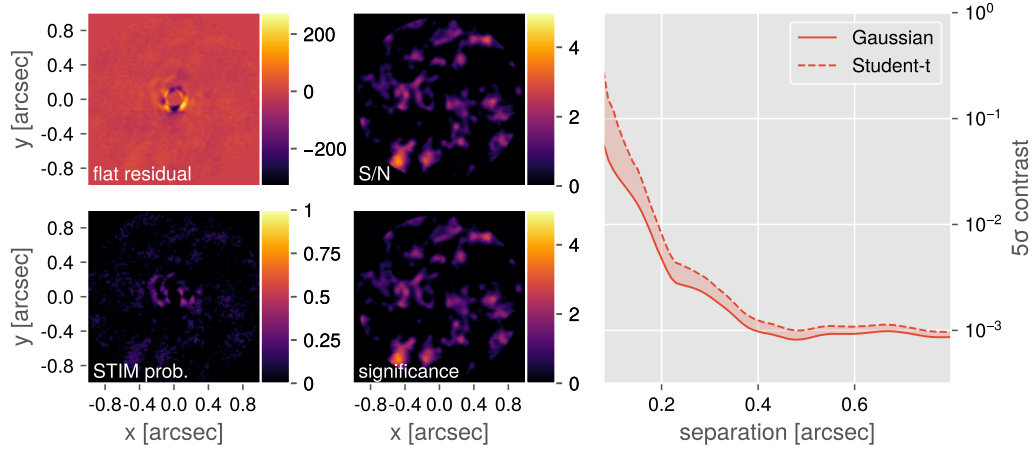


Figure 10. Post-processing results from the second epoch using full-frame median subtraction. The top-left frame is the collapsed residual frame, the top-right is the Gaussian S/N map, the bottom-left is the STIM probability map, and the bottom-right is the Student-t corrected significance map. In each frame the inner FWHM is masked out. The right figure show the Gaussian (solid line) and Student-t corrected (dashed curve) 5σ contrast curve. Outputs for other epochs and other algorithms (21 figures) are in the online figure set and the GitHub repository.

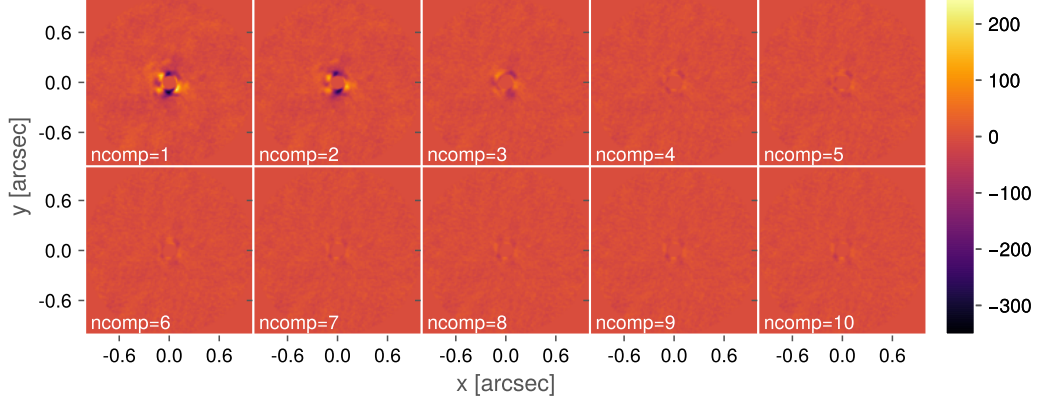


Figure 11. Collapsed residual frames from the first epoch using PCA reduction with 1-10 components. The figures share a common scale and the inner FWHM is masked out for all the frames. Outputs for the other epochs and for the NMF and GreeDS algorithms (9 figures) are in the online figure set and the GitHub repository

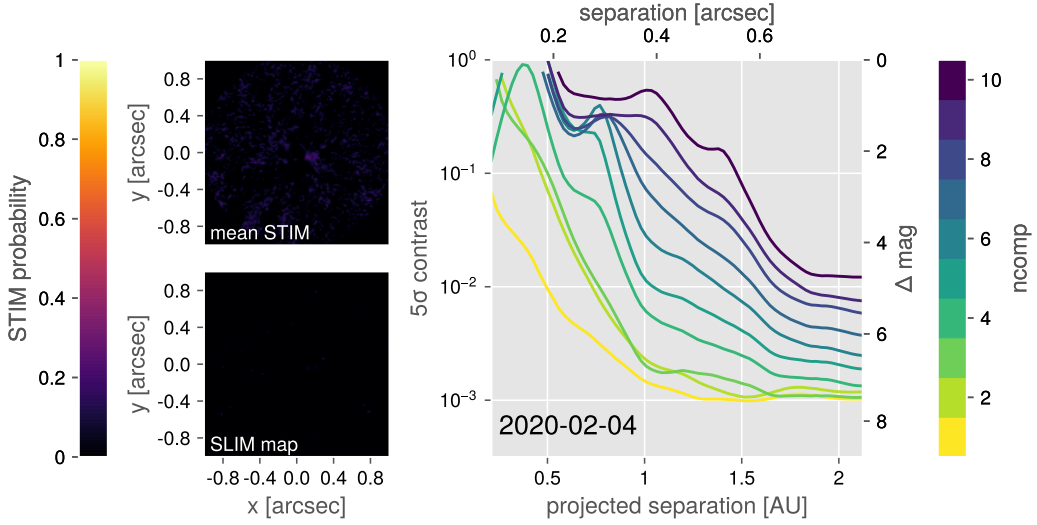


Figure 12. 5σ Gaussian contrast curves for the first epoch using PCA reduction with 1-10 components. The left two figures are the average STIM probability map, and the SLIM detection map. For both of these maps, a typical cutoff value is 0.5. Outputs for the other epochs and for the NMF and GreeDS algorithms (9 figures) are in the online figure set and the GitHub repository.

B. PROVISIONAL ORBIT FITTING

We found multiple interesting blobs in the reduced data that were not statistically significant. Nonetheless, we tried fitting Keplerian orbits using OFTI to determine the feasibility of the blobs being real companions. We began by estimating the astrometry of the blobs by eye in reduced data (Table 2, Figure 13). We tried simulating 10^4 orbits via rejection sampling with OFTI but failed to constrain all three points with any one orbit. Overall we determine these blobs are not real companions and are most likely systematic noise in the stellar PSF.

Table 2. Provisional astrometry for blobs of interest from each epoch. The separation and offset are in relation to Sirius B. The uncertainties are derived from the FWHM of the PSF from each epoch.

Date observed	offset (mas)	PA ($^{\circ}$)
2020-02-04	114 ± 40	-115 ± 20
2020-11-21	121 ± 38	-119 ± 18
2020-11-28	114 ± 41	-113 ± 21

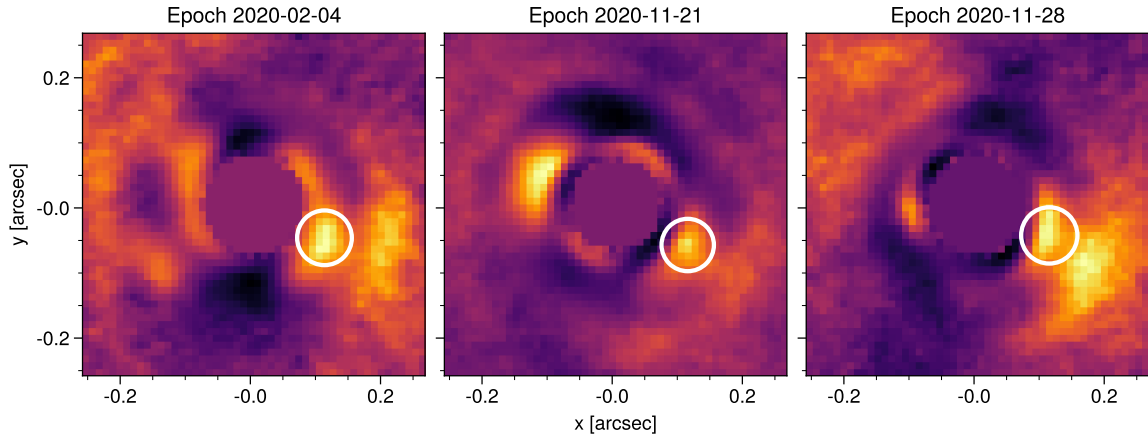


Figure 13. Provisional astrometry (white circles) displayed on STIM maps using the GreeDS algorithm with 2 components. Each frame was cropped to the inner $0.25''$ and the inner FWHM has been masked out. The width of the circles represent the uncertainty.